Journal of Solid State Chemistry 184 (2011) 3262–3268

Contents lists available at SciVerse ScienceDirect

Journal of Solid State Chemistry

journal homepage: www.elsevier.com/locate/jssc

Synthesis, crystal structure and physico-chemical properties of the new quaternary oxide $Sr_5BiNi_2O_{9.6}$

Mariya Novitskaya [a], Leonid Makhnach [a], Ludmila Ivashkevich [b], Vladimir Pankov [a], Holger Klein [c], Amélie Rageau [c], Jérémy David [c,1], Mauro Gemmi [c,d], Joke Hadermann [e], Pierre Strobel [c,*]

[a] Department of Chemistry, Belarus State University, 14 Leningradskaya Str., 220030 Minsk, Belarus
[b] Institute of Physicochemical Problems, Belarus State University, 14 Leningradskaya Str., 220030 Minsk, Belarus
[c] Institut Néel CNRS and Université J. Fourier, BP 166, 38042 Grenoble Cedex, France
[d] Center for Nanotechnology Innovation, NEST Istituto Italiano di Tecnologia, Piazza S.SIlvestro 12, 56127 Pisa, Italy
[e] Electron Microscopy for Materials Research (EMAT), University of Antwerp, Groenenborgerlaan 171, B-2020, Antwerp, Belgium

ARTICLE INFO

Article history:
Received 24 August 2011
Received in revised form
4 October 2011
Accepted 4 October 2011
Available online 18 October 2011

Keywords:
Perovskite
Solid state synthesis
Nickelates
Oxygen vacancies

ABSTRACT

A new black quaternary oxide $Sr_5BiNi_2O_{9.6}$ was synthesized by solid state reaction at 1200 °C. Its structure was solved by electron crystallography and X-ray powder refinement, yielding a tetragonal structure with space group $I4/mmm$, $a=5.3637$ (2) Å, $c=17.5541(5)$ Å, $Z=4$. The structure can be described as a stacking of (Bi,Sr)–O rocksalt slabs and $SrNiO_{3-\delta}$ perovskite slabs. The initial nickel valence is close to +3.1. Thermogravimetry and high-temperature oxygen coulometry showed that this compound has variable oxygen content as a function of temperature and oxygen pressure, and ultimately decomposes when heated in low oxygen pressure above 800 °C. It is a metallic conductor with n-type conduction. Its thermoelectric power was determined and found to be −20 and −38 μV/K at 300 and 650 °C, respectively. Magnetic measurements confirm the nickel valence close to +3 and show evidence of magnetic ordering at 20 K.

1. Introduction

The search for new compounds containing transition metals and large cations has given rise to the discovery of many interesting materials. The key structural models in this area are perovskite and K_2NiF_4 structures, with various vacant sites and intergrowth possibilities. The most famous examples of such compositions are the superconducting cuprates. Since then a number of similar compounds containing bismuth, alkaline-earth and transition metal cations M have been reported. The tolerance of perovskite-related structures to various cationic substitution in both A and B sites opened the road to the synthesis of numerous new mixed oxides with remarkable thermoelectric or electrochemical (fuel cells) properties, especially with M=Mn or Co [1–5]. By now several studies with M=Cu [6–8], Fe+Cr [9] were published. Oddly enough, nickel-containing systems have been little studied so far, in spite of the considerable interest generated by the (La,Sr)–Ni–O system [10,11]. In this paper, we report a new phase discovered in the Sr–Bi–Ni–O system, and its full crystallographic characterization, which has been made possible by a combination of X-ray and electron diffraction techniques. Electrical and thermoelectric properties were also determined.

2. Experimental

The target stoichiometry in this study was $Sr_3B_2O_x$ with B=Ni, Bi, considering the possible formation of a Ruddlesden–Popper structure. Several $Sr_3Bi_{2-x}Ni_xO_{6-\delta}$ nominal composition were prepared by solid state synthesis, starting from reagent grade $Sr(NO_3)_2$, $Bi(NO_3)_3\cdot 6H_2O$ and $Ni(NO_3)_2\cdot 6H_2O$. The nitrates were mixed in appropriate ratios and dissolved in a small amount of distilled water. 2–5 ml of concentrated nitric acid was added to ensure effective dissolution of bismuth nitrate. The aqueous solution was evaporated by heating from room temperature to 300 °C and held for 2 h at this temperature. The resulting precursor was ground in an agate mortar, then hydrostatically pressed as a pellet and fired in air at 700–750 °C for 5 h. The product was subsequently calcined in air or in oxygen 15 h at 900 °C then 24 h at 1000–1200 °C with intermediate grinding and compacting. Samples were furnace-cooled (cooling rate 100–150 °C/h) in all thermal treatments.

Diffraction patterns of powdered samples were recorded at room temperature on an X-ray diffractometer HZG 4A (Carl Zeiss,

---

[*] Corresponding author. Fax: +33 476 88 7940.
E-mail address: pierre.strobel@grenoble.cnrs.fr (P. Strobel).

[1] Present address: LSPCTS, Centre Européen de la Céramique, 12 rue Atlantis, 87068 Limoges, France.

0022-4596/$ - see front matter © 2011 Elsevier Inc. All rights reserved.
doi:10.1016/j.jssc.2011.10.020

Jena) equipped with Cu$K\alpha$ anode, Ni filter, receiving detector slit 0.22 mm, and Soller slits on the primary beam. Acquisition conditions were $8.5^\circ \leq 2\theta \leq 130^\circ$, step size 0.02°, counting time 15 s/step. Rietveld refinements were carried out using the Fullprof program [12], using a Pseudo-Voigt profile function and a 6-term polynomial fit for the background. The asymmetry of the reflections profile (up to $2\theta = 25^\circ$) and preferred orientation (using Marsh-Dollas function [13,14]) were taken into account. Variables in the refinements were cell parameters, atomic coordinates, atomic displacement parameters B_{iso} for all atoms except oxygen ones, the scale factor, profile parameters U, V, W, η, the preferred orientation and asymmetry parameters. Global parameters included were the zero displacement and the polynomial background coefficients. The molecular graphic was drawn using ORTEP-3 (Calidris Co., Sweden).

For transmission electron microscopy (TEM) studies, diffraction patterns in standard selected area mode (SAED) and in precession mode were obtained in a Philips CM300ST operated at 300 kV and equipped with a Spinning Star (Nanomegas) precession unit. The chemical analysis was performed by energy dispersive X-ray spectroscopy (EDS) on a JEOL 840 scanning electron microscope operated at 20 kV. In order to correlate chemical composition to crystal structure (cf. below), EDS analysis was also carried out at Earth Science Department, University of Milano, Italy, on a TEM Teenai F20ST equipped with an EDAX spectrometer. High resolution micrographs (HRTEM) were obtained on a JEOL 4000EX microscope. The image simulations were made using the MacTempas software.

Thermal analysis was performed on a Netzsch STA-409 therma analyzer, using alumina crucibles in static air atmosphere in the range 20–1000 °C. The temperature variation rate was 10 °C/min. The sensitivity of the thermobalance is 2 μg.

The oxygen content of a single-phase was determined by iodometric titration and by high-temperature coulometric reduction of the samples. The latter was achieved using an OXYLYT system (Sensotech, Magdeburg, Germany), which allows to determine the amount of released and adsorbed oxygen. This measurement was carried out on 50–100 mg samples at 1000 °C in argon. The electrical conductivity was measured using a standard DC four-point method on parallelipipedic sintered samples. The measuring head was placed in a controlled-temperature furnace, and a heating/cooling rate of 2.6°C/min was used.

The Seebeck coefficient α was determined using silver electrodes and a temperature gradient between hot and cold ends of the sample $\Delta T = 10$–15 K. α was calculated as $\alpha = \Delta E/\Delta T$, where ΔE is the measured thermoelectric electromotive force between the hot and the cold end. Experimental values of α were corrected taking into account the Seebeck coefficient of silver.

Magnetic properties were measured in the range 2–300 K in a superconducting quantum interference device (SQUID) magnetometer in magnetic fields of 100 Oe, using a powder encapsulated in tightly wrapped polyethylene foil. Zero-field cooled and field-cooled data were recorded. Magnetization vs. field curves were checked at various temperatures between 5 and 300 K.

3. Results and discussion

3.1. Structural characterization

3.1.1. Preliminary characterization

The XRD diffraction pattern obtained for nominal composition $Sr_3Bi_{0.6}Ni_{1.4}O_x$ could be indexed in a body-centered tetragonal unit cell with $a = 5.362$ Å, $c = 17.524$ Å (from 23 indexed reflections). A SEM examination on sintered blocks revealed a dense ceramic that is almost single-phase. EDX analysis shows that the majority phase has a composition close to Sr:Bi:Ni = 5:1:2 (average of 12 measured points). A few nickel-poor areas were found, with average composition Sr:Bi:Ni = 8.5:3:1.

3.1.2. Electron crystallography study

Given the absence of literature data in this quaternary system and the complexity of the observed diffractogram, a structural model was sought using electron diffraction. A detailed examination of numerous crystallites showed that the sample contained three different phases: a majority tetragonal phase compatible with the above-mentioned cell parameters, an orthorhombic phase with cell parameters $a \approx 3.8$ Å, $b \approx 7.5$ Å and $c \approx 18.2$ Å, and a minority phase with a large unit cell. Since the cell parameters of the orthorhombic phase are closely related to those of the tetragonal phase ($a_o \approx a_t/\sqrt{2}$, $b_o \approx a_t * \sqrt{2}$, $c_o \approx c_t$), only few zone axes allowed to distinguish these two phases from each other. In order to avoid ambiguities due to intensities originating from particles of different phases, in the following only data collected on a single particle clearly identified as the I-centered tetragonal phase are considered.

A total of 13 different zone axes were recorded in SAED mode and with 4 different precession angles (1.25°, 2.3°, 3.4° and 4.1°). For each zone axis the optimum precession angle was chosen in terms of diminishing multiple diffraction effects without suffering from overlap of different Laue zones. The optimum precession angle turned out to be 2.3° for all zone axes except for [1 1 1] where a precession angle of 3.4° was used. Diffracted intensities were extracted from the zone axes by the program ELD of the CRISP suite and the data from different zone axes were merged into one 3-dimensional data set using the Triple program (all software from Calidris Software, Sollentuna, Sweden). The data were then corrected by a Lorentz-type factor taking into account the acquisition geometry [15]. The intensities were treated in the pseudo-kinematic approximation, i.e. assuming that the diffracted intensities are proportional to the square of the structure factors [15]. We used the structure factors extracted from the 8 main zone axes ([0 0 1], [0 1 1], [0 2 1], [1 1 1], [−1 1 1], [−1 3 1], [1 5 −1] and [1 7 −1]). This yielded a total of 109 independent reflections with a resolution of 0.8 Å (see Fig. 1).

The extinction conditions and intensity symmetries observed in the zone axes lead to possible space groups $I4/mmm$ or $I4mm$. EDX on a tetragonal phase grain yielded a 64:14:22 Sr:Bi:Ni atomic ratio (oxygen was too light to be reliably determined). This information was introduced into the SIR 2008 program for structure solution. Since no significant difference was observed between the structure solutions in the non-centrosymmetric group $I4mm$ and in the centrosymmetric one $I4/mmm$, the latter was retained. These data yielded a structure with a reliability factor $R = 29\%$ and reasonable interatomic distances and coordination polyhedra, except for an empty space at the center of the cell edge along the a direction where crystal chemistry considerations would indicate a possible oxygen position (O1 in Table 1). In a first approximation (cation mixing neglected), this model lead to a stoichiometry $Sr_5BiNi_2O_x$.

3.1.3. Powder X-ray diffraction—structure description

These results prompted us to prepare a new sample with 5:1:2 Sr:Bi:Ni ratio. This sample was used for all further measurements. The Rietveld refinement of its XRD pattern fully confirmed the solution reached above (see Table 1 and Fig. 2). The presence of O1 atom at 1/2 0 0 was also confirmed. Main cation–anion distances are given in Table 2, and a drawing of the structure is given in Fig. 3.

This structure is isotypic with that described previously by Pelloquin et al. in the Sr–Bi–M–O systems (M = Cr, Fe or Mn, with

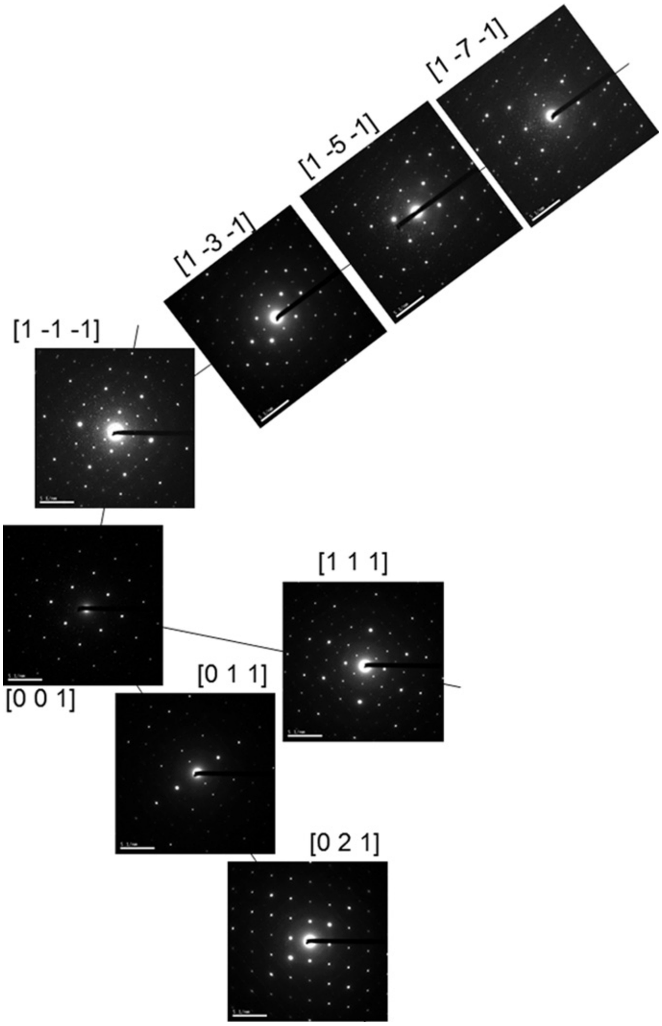

Fig. 1. Precession electron diffraction patterns of the 8 zone axes used for the structure solution by electron crystallography. The precession angle is 2.3° for all zone axes except 3.4° for [1 1 1].

a superstructure in the latter case) [7,8]. It can be described as a stacking of rocksalt-type and perovskite-type layers along *c*, corresponding to a "1201" structure in the superconducting bismuth cuprates terminology. The cations follow a stacking of successive layers (Sr,Bi)–Sr–Ni–Sr–(Sr,Bi)… along *c*. In the layer at $z=0$, all atoms are in special positions and form a perfectly square $SrBiO_2$ lattice; we found no evidence of a significant shift of atom O1 from the 4*c* special position, as reported previously for $M=$Cr and Fe (but not for Mn). Nickel, bismuth and Sr1 are octahedrally coordinated by oxygen atoms with O–*M*–O angles equal or very close to 90° (89–91° for the nickel site). The Sr2 atoms links the rocksalt-like (Sr,Bi)–O block and the perovskite-like Ni–O one, yielding a more complex environment with nine oxygen neighbors (see Fig. 3). The Sr1 site is especially distorted, since it forms two short apical bonds to O3 and 4 long planar ones to O1 (see Table 2).

Cation vacancies or mixing were found negligible on all cation sites. This compound differs in this respect from "1201" phases with $M=$Fe, Cr or Mn where Bi–*M* or Bi–Sr mixing was found [7,8]. Within the limited accuracy of XRD data on light atom occupations, oxygen vacancies have been found mainly on the O4 site, i.e. in the nickel-containing planes at $z\approx 1/4$, and are also possible in the O1 site (see Table 1). The refinement of oxygen occupations yields the formula $Sr_5BiNi_2O_{9.54}$, showing that nickel is close to trivalent in this compound (the charge balance for pure Ni^{3+} would lead to 9.50 O atoms/formula). Such a nickel valence v(Ni) is consistent with the fact that this compound is black. It is in good agreement with iodimetric titration yielding a formula unit $Sr_5BiNi_2O_{9.64}$ with v(Ni)$=+3.14$, and with thermogravimetry data (see next section). In the following, the formula of this new phase will be named $Sr_5BiNi_2O_{9.6}$ for simplicity.

3.1.4. *High-resolution electron microscopy*

HREM images taken along the [1 0 0] direction of the unit cell confirm the layer nature of the structure (see Fig. 4). At this defocus value, the perovskite (NiO_2) layers are visible as continuous lines on the thinner part of the crystallite (top of Fig. 4) and rows with a dashed aspect in the thicker part (bottom of Fig.4) . Theoretical HRTEM images calculated at a focus value $f=-10$ nm

Table 1
Refined structural data for $Sr_5BiNi_2O_{9.6}$ (ED/XRD=electron/X-ray diffraction).

General data		**Statistical parameters for Rietveld refinement**	
Space group	*I*4/*mmm* (No.139)	No. reflections	168
Cell parameters		No. refined parameters	28
a (Å)	5.3637(2)	N–P+C	6048
c, Å	17.5541(5)	R_p	0.026
V (Å^3)	505.03(5)	R_{wp}	0.040
Z	4	R_{exp}	0.031
hkl of texture	00l	χ^2	1.67
G_1 (texture)	0.565(1)	R_B	0.052
G_2 (texture)	0	R_F	0.053

Atomic parameters

Atom	Wykoff position	*x*	*y*	*z (ED)*	*z (XRD)*	B_{iso}, *Å^2 (XRD)*	*Occupation*
Bi	2a	0	0	0	0	1.05(12)	1
Sr1	2b	0	0	0.5	0.5	0.8(2)	1
Sr2	8g	0.5	0	0.151	0.1500(1)	1.0(1)	1
Ni	4e	0	0	0.250	0.2519(4)	1.8(2)	1
O1	4c	0.5	0	0	0	0.8(3)[a]	0.96(3)
O2	4e	0	0	0.127	0.137(1)	0.8(3)[a]	1
O3	4e	0	0	0.6259	0.624(1)	0.8(3)[a]	1
O4	8f	0.25	0.25	0.25	0.25	0.8(3)[a]	0.905(15)

[a] Constrained to an equal value.

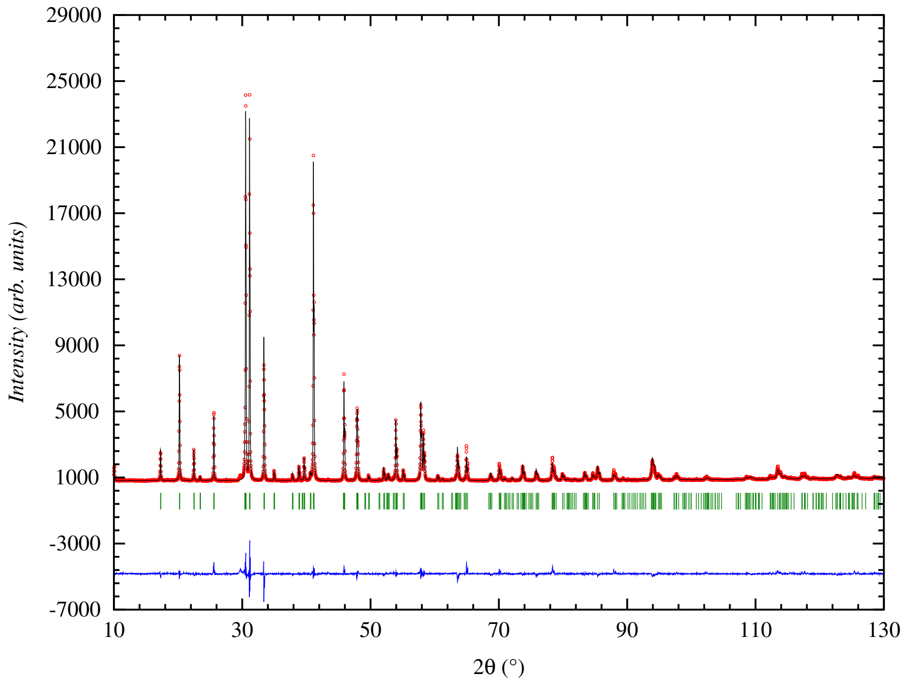

Fig. 2. Experimental (dotted line), and calculated (continuous line) profiles of $Sr_5BiNi_2O_{9.6}$ after refinement by the Rietveld method. The lower line is the difference $I_{obs}-I_{calc}$. Reflections are indicated by vertical bars.

Table 2
Main interatomic distances in $Sr_5BiNi_2O_{9.6}$.

Atom pair	Distance (Å)	*n*
Bi–O1	2.6819	× 4
Bi–O2	2.398	× 2
Sr1–O1	2.6819	× 4
Sr1–O2	2.171	× 2
Sr2–O1	2.6331	× 1
Sr2–O2	2.6922	× 2
Sr2–O3	2.7213	× 2
Sr2–O4	2.5842	× 4
Ni–O2	2.023	× 1
Ni–O3	2.183	× 1
Ni–O4	1.8967	× 4

and thicknesses of two unit cells for the thin part and 23 unit cells for the thicker part are placed inside the image and are in good agreement with the experimental image.

4. Physico-chemical properties

4.1. Oxygen desorption–absorption

A thermogravimetric investigation showed that $Sr_5BiNi_2O_{9.6}$ loses oxygen when heated above 400 °C in argon. Two main oxygen losses occurred with peaks in DTG in the 400–600 and 850–950 °C ranges (see Fig. 5).

The oxygen extraction–absorption process in $Sr_5BiNi_2O_{9.6}$ was then investigated using the coulometric system OXYLYT [16] under variable oxygen partial pressure. This system has two main advantages compared to thermogravimetry: (1) it selectively measures the absorption/desorption process of oxygen only, thanks to the use of oxygen sensors, (2) it can be run with variable and controlled partial pressure of oxygen. The sample was heated at 7°C/min from room temperature to 1000°C, held at this temperature until equilibrium with the gaseous phase was reached, and then cooled at 7 °C/min. This process was carried out on a sample previously annealed in air in the same temperature conditions.

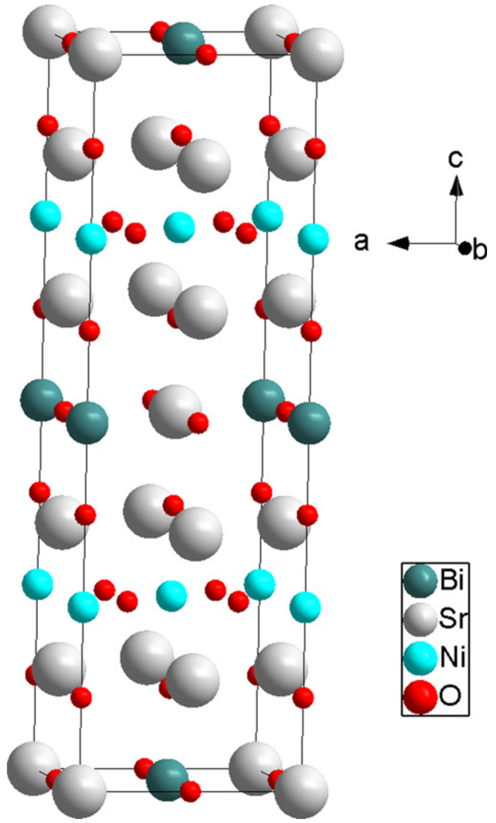

Fig. 3. $Sr_5BiNi_2O_{9.6}$ crystal structure: (a) perspective view and (b) detailed view of the Sr2 environment.

The experimental oxygen desorption/absorption results are presented in Fig. 6 in the form of the titration current of the

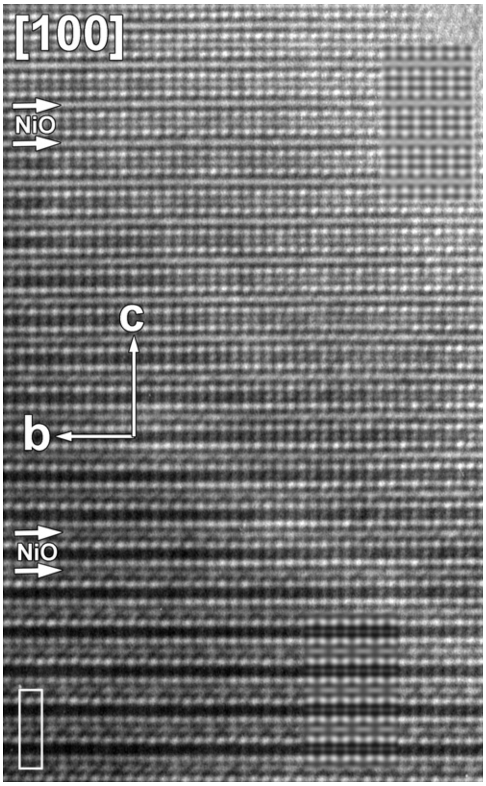

Fig. 4. HRTEM image of the [1 0 0] zone of $Sr_5BiNi_2O_{9.6}$. The white arrows indicate the position of the perovskite (NiO_2) layers. Theoretical HRTEM images are inserted at the top right and bottom right of the image.

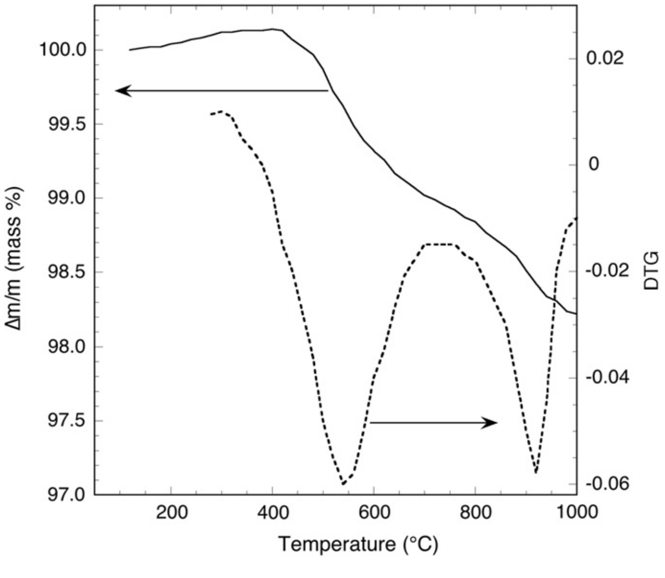

Fig. 5. Thermogravimetric behavior $Sr_5BiNi_2O_{9.6}$ in argon (full line: relative mass variation, dashed line: derivative of mass variation with temperature).

coulometric cell as a function of time. In this section, oxygen partial pressures are expressed in ppm, where “ppm” means $10^6 \times p(O_2)/P(\text{total})$, so that 490 ppm, for instance, means a partial pressure of oxygen in air of 490×10^{-6} atm. This measurement shows that no oxygen exchange takes place below 400 °C. It is followed by a considerable oxygen loss in the temperature range 400–600 °C (“A” peak). Additional oxygen loss peaks (“B”) are observed in the 800–850 and 900–950 °C ranges. Note that these features are in excellent agreement with thermogravimetry data.

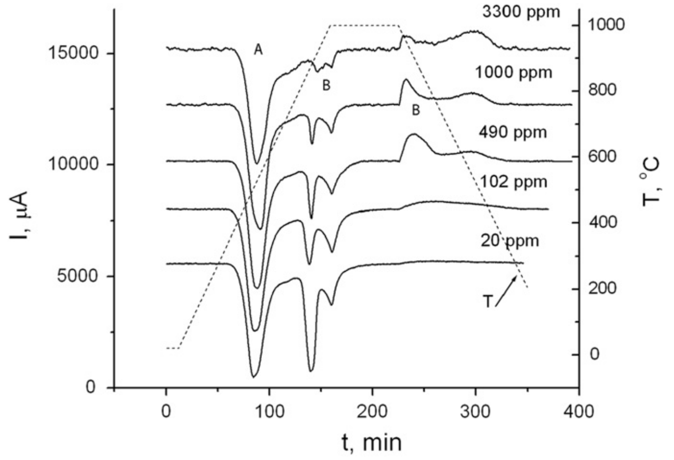

Fig. 6. Coulometric oxygen desorption/absorption titration curves as a function of temperature (dashed line and right-hand scale) and of oxygen partial pressure (20–3300 ppm).

On cooling, oxygen re-absorption is observed in the temperature range 1000–800 °C at oxygen partial pressures $p(O_2) \geq 490$ ppm. This broad re-absorption peak correlates well with the double desorption B peak observed on heating in the same range, showing that the B phenomenon is reversible when the oxygen pressure is not too low. Unlike the irreversible peak A, the B peak areas depend strongly on oxygen pressure ; the lower the oxygen pressure, the larger the peak area of the B reaction. The fact that the reverse reaction is not observed at low oxygen pressure (102 or 20 ppm) can be due to two effects: (1) difficulty to reach thermodynamic equilibrium at the gas–solid interface at low $p(O_2)$, (2) a decrease in oxygen diffusion mobility at low oxygen content.

The fact that the coulometric titration measurement detects three peaks show that desorption is due to different types of oxygen atoms, characterized by different crystal lattice bonding energies. Going back to the atomic arrangement in $Sr_5NiBi_2O_{9.6}$, we note that it can be described as a combination of two types of structural units, a NaCl-type block and a perovskite-type block, containing Bi–Sr–O and Ni–Sr–O atoms, respectively. The structure is built up as a sequence $(Bi_{0.5}Sr_{0.5})O$–SrO–$SrNiO_{3-\delta}$. In this lattice, the $SrNiO_{3-\delta}$ perovskite layer can accommodate large oxygen vacancies that are also favored by the variable valence of Ni atoms. In a previous study of oxygen absorption/desorption processes in $Ln_{2-x}Sr_xNiO_4$ nickelates (Ln=La, Ce, Nd, Eu) with high strontium concentration, i.e. high nickel valence, we showed evidence of oxygen loss at $T \sim 500$ °C [10]. This process is likely to correspond to the 400 °C desorption of oxygen from the atoms lying in the nickel planes in the $Sr_5NiBi_2O_{9.6}$ (O4 site, see Fig. 3), which have the lowest crystal lattice bonding energy. The formation of oxygen vacancies in perovskite layers is rather common and is known to lead to superlattices when oxygen vacancies in the M transition metal equatorial plane occur in an ordered manner, as in brownmillerite or in $LaNiO_{2.5}$ [17,18].

Since the initial nickel valence ν_{Ni} is ≈ 3.10, it is not surprising to detect a partial nickel reduction with oxygen loss on heating in oxygen-poor atmosphere. Note that thermogravimetry yields mass losses corresponding to 0.64 and 0.46 O atoms per formula unit in the ranges 400–700 °C and 700–1000 °C, respectively. Such mass losses, if due to oxygen vacancies, bring the nickel valence to +2.5 at 700 °C and +2.04 at 1000 °C, in agreement with a two-step reduction of nickel correlated with formation of oxygen vacancies. It is interesting to note that the stability “plateau” between the A and B reactions found by thermogravimetry and oxygen coulometry corresponds to $\nu(\mathrm{Ni})=2.5$ exactly. This would correspond to 25% oxygen vacancies on the O4 site.

In order to confirm the identification of the "B" coulometric peaks at high temperature, additional experiments were carried out. A sample of $Sr_5BiNi_2O_{9.6}$ was placed in a quartz cell, from which air was pumped down to a vacuum of 10^{-2} Torr. After this treatment other phases were found, in particular a non-conducting phase with a composition close to $Sr_3BiNi_{0.7}O_y$ and NiO, and only trace amounts of $Sr_5BiNi_2O_{9.6}$. If the sample is re-annealed later in oxygen at 1050–1100 °C, the $Sr_5BiNi_2O_{9.6}$ phase is recovered. This reaction mechanism with formation of lower-valent NiO is consistent with thermogravimetric data and with the fact that the reaction is strongly enhanced when the oxygen partial pressure is decreased. These results also show that the new $Sr_5BiNi_2O_{9.6}$ phase is not stable under low oxygen pressure conditions leading to the loss of more than 25% oxygen atoms from the O4 site.

The thermal behavior of $Sr_5BiNi_2O_{9.6}$ can be summarized by the following reactions:

$$Sr_5BiNi^{3.1+}{}_2O_{9.6}\xrightarrow{\approx 400^\circ C}Sr_5BiNi^{2.5+}{}_2O_9+0.3O_2\uparrow \quad (A)$$

$$Sr_5BiNi^{2.5+}{}_2O_9\xrightarrow{850-1000^\circ C}Sr_3BiNi^{2+}{}_{0.7}O_y+(Sr,Bi)O_x+1.3Ni^{2+}O+0.25O_2\uparrow \quad (B)$$

4.2. Electrical conductivity

Fig. 7 presents the dependence of the resistivity of $Sr_5BiNi_2O_{9.6}$ with temperature during heating and cooling in air. From results described in Section 4.1, we expect this measurement to be strongly influenced by oxygen stoichiometry and nickel valence changes on heating. Below 220 °C, $\rho(T)$ increases weakly with temperature, i.e. behaves as a metallic conductor, and is roughly constant in the temperature range 220–420 °C. From this temperature on, a sharp rise is observed until ca. 750 °C, followed by a resistivity decrease at higher temperature. The sharp resistivity increase in the 420–750 °C is likely to be connected with oxygen desorption, which occurs in the same temperature range. We assume that the resistivity increase is related to vacancy ordering such as that observed in the brownmillerite case. This is all the more plausible as the 600–800 °C range corresponds to a fixed composition ($\nu_{\mathrm{Ni}}=+2.5$) and O4 vacancy fraction (1/4 exactly), and as this can also result in charge ordering of nickel cations. Above 750 °C, we know that more vacancies occur and the compound finally decomposes. The presence of such ordered vacancies, which can be retained on cooling, can explain the hysteresis of the curve presented in Fig. 7. This behavior is reminiscent of that of K_2NiF_4-type nickelate $La_{0.6}Sr_{1.4}NiO_{4-\delta}$, where a correlation between resistivity and oxygen vacancy concentration was recently demonstrated [10].

4.3. Thermolectric power

Fig. 8 shows the temperature dependence of the thermoelectric power of $Sr_5BiNi_2O_{9.6}$. This material is a n-type conductor in the range of temperature from room temperature to 1100 K. The temperature variation of the Seebeck coefficient, with a wide maximum around 650 K, is reminiscent of that observed previously in K_2NiF_4-type nickelates such as $La_{2-x}Sr_xNiO_{4\pm\delta}$ [19–21]

This shows that the electroconductive properties of Sr5BiNi2O8 $\pm\delta$ depend mainly on theperovskite nickel-containing layers. In the 20–400 °C temperature range, α varies rather linearly with temperature and increases from -18 to -37 μV/°, which indicates an increase in electron mobility. At higher temperature, the oxygen loss leads to decrease of electron mobility and α decreases with increasing temperature.

4.4. Magnetic properties

The temperature dependence of the molar susceptibility of $Sr_5BiNi_2O_{9.6}$ is shown in Fig. 9. The variation of the inverse susceptibility with temperature $\chi^{-1}(T)$ (Fig. 9b) departs from linearity at rather high temperature, showing the occurrence of strong magnetic interactions. A clear magnetic ordering transition occurs at 20 ± 1 K. No significant difference between zero-field cooled and field-cooled data occurs at low temperature (Fig. 9a). The shape of the $\chi^{-1}(T)$ curve points to dominant antiferromagnetic interactions. A ferromagnetic component, however, is visible in the $M(H)$ dependence at 5 K (see Fig. 9c). A Curie–Weiss law $\chi=C/(T-\theta)$ was tentatively fitted to data in the range 230–300 K. The experimental slope corresponds to a Curie constant of 1.894. In the spin-only scheme usually followed by 3d cations (assuming

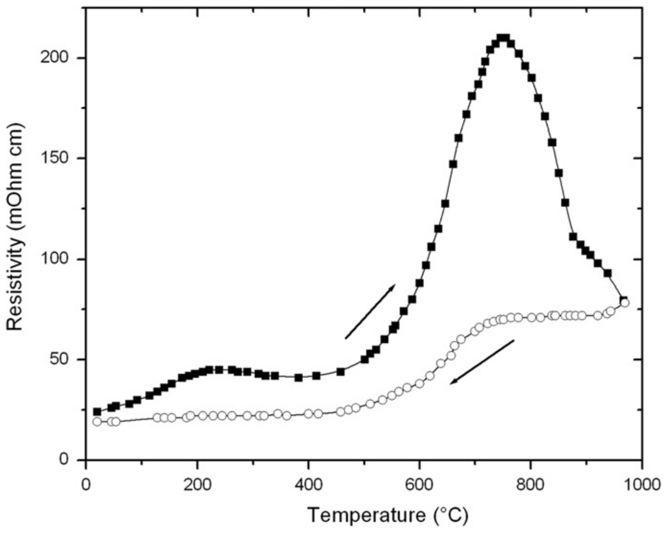

Fig. 7. Variation of resistivity of $Sr_5BiNi_2O_{9.6}$ on heating (full points) and cooling (open points). Heating/cooling at rate 2.6 °C/min in air.

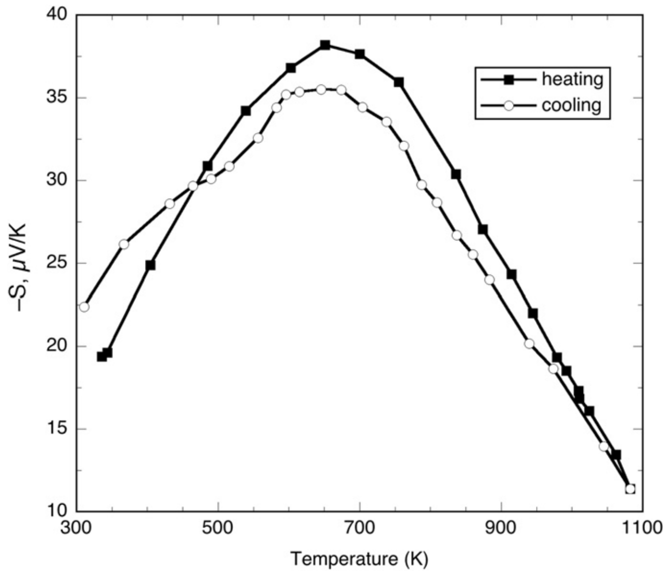

Fig. 8. Temperature dependence of the thermoelectric power of $Sr_5BiNi_2O_{9.6}$.

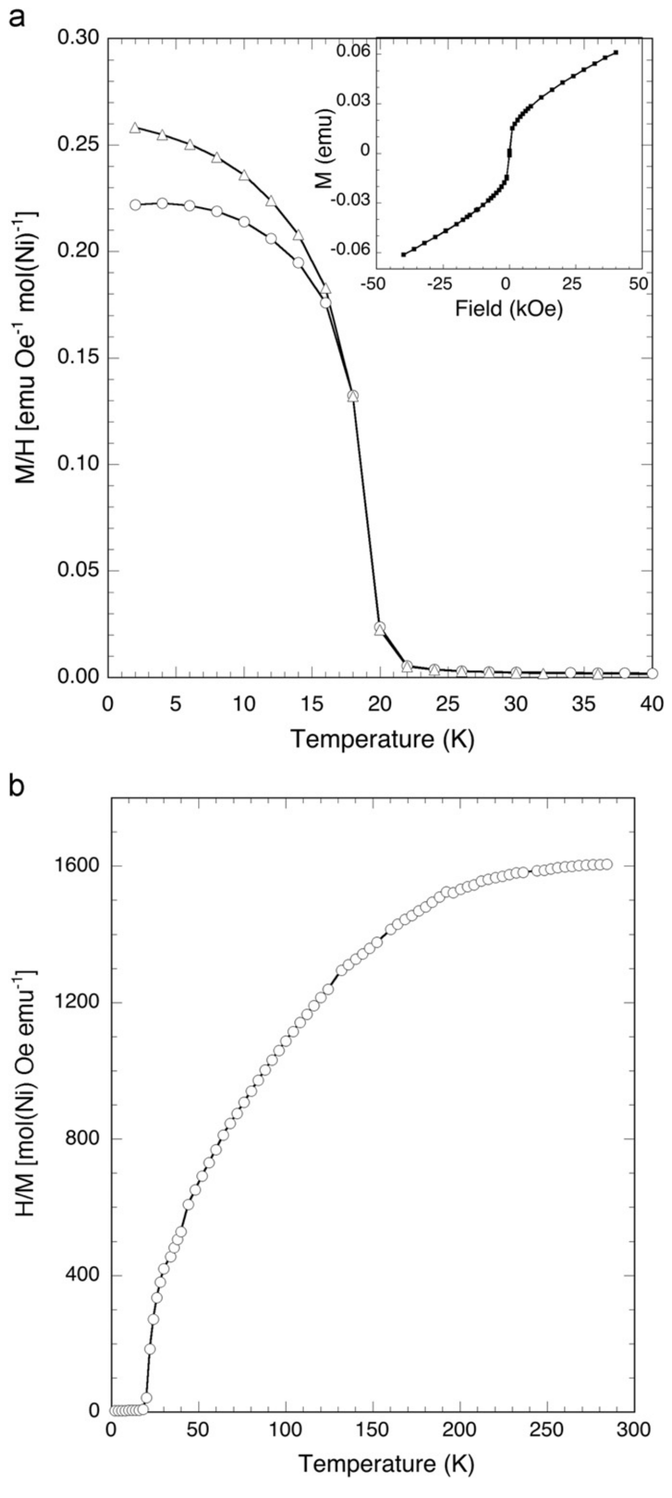

Fig. 9. Magnetic properties of $Sr_5BiNi_2O_{9.6}$: (a) low-temperature field-cooled and zero-field cooled susceptibility $\chi = M/H$ measured with $H = 100$ Oe (inset: $M(H)$ variation at 5 K); (b) reciprocal susceptibility vs. temperature ($H = 100$ Oe). All data are normalized to 1 mol Ni.

complete quenching of the orbital momentum), the effective magnetic momentum is given by

$$\mu_{\text{eff}} = g[S(S+1)]^{1/2}\mu_B$$

where μ_B is the Bohr magneton and $g \approx 2.0$. For Ni^{3+} (a d^7 cation), the expected high-spin configuration yields μ_{eff}/μ_B (theor) = 3.87. An experimental value of μ_{eff} can be calculated from the Curie constant using the equation:

$$\mu_{\text{eff}}/\mu_B = \sqrt{(3k_B/N)}$$

where k_B is the Boltzmann constant and N is Avogadro's number. Using $C = 1.894$, we obtain $\mu_{\text{eff}}/\mu_B = 3.89$, in excellent agreement with the theoretical value for Ni^{3+}.

5. Conclusions

In this work, we achieved the preparation of a new quaternary Sr–Bi–Ni–O tetragonal phase. Its crystal structure was solved, thanks to a combination of precession electron diffraction, HRTEM and powder diffraction techniques. It consists of a combination of NaCl-type and perovskite-type layers stacked along the tetragonal *c*-axis. This new black Ni^{3+} compound loses oxygen depending on temperature and partial pressure of oxygen. Resistivity, thermoelectric power and magnetic properties of this new oxide are reported. The high-temperature $\rho(T)$ dependence is complex because of the oxygen desorption/absorption vs. temperature. Magnetic measurements confirm the presence of Ni^{3+} and indicate magnetic ordering below 20 K, which should be investigated in the next future by neutron diffraction.

Acknowledgments

We wish to thank Sebastien Pairis (Institut Neel, Grenoble) and A.M. Abakumov (EMAT, University of Antwerp) for their assistance in EDX measurements and interpretation of X-ray data, respectively. The authors gratefully acknowledge the financial support of NATO (Project CLG 982009).

References

[1] J.M. Tarascon, R. Ramesh, P. Barboux, M.S. Hedge, G.W. Hull, L.H. Greene, Y. LePage, W.R. McKinnon, J.V. Waszcak, L.F. Schneemeyer, Solid State Commun. 71 (1989) 663–668.
[2] D. Pelloquin, C. Michel, A. Maignan, M. Hervieu, B. Raveau, J. Solid State Chem. 138 (1998) 278–289.
[3] D. Pelloquin, A.C. Masset, A. Maignan, M. Hervieu, C. Michel, B. Raveau, J. Solid State Chem. 148 (1999) 108–118.
[4] D. Pelloquin, A. Maignan, M. Hervieu, C. Michel, B. Raveau, J. Solid State Chem. 151 (2000) 210–219.
[5] D. Sedmidubsky, M. Nevriva, J. Leitner, Thermochim. Acta 450 (2006) 38–41.
[6] K. Kudo, T. Nishizaki, N. Okumura, N. Kobayashi, J. Phys. Chem. Solids 69 (2008) 3022–3026.
[7] C.H. Wu, Y.C. Chu, D.C. Ling, S.H. Liu, W.F. Pong, H.S. Hseu, J.M. Chen, J.F. Lee, H.C.I. Kao, Physica C 460–462 (2007) 422–423.
[8] H.Q. Luo, L. Fang, M. Gang, H.H. Wen, J. Crystal Growth 305 (2007) 222–227.
[9] M. Allix, D. Pelloquin, F. Studer, N. Nguyen, A. Wahl, A. Maignan, B. Raveau, J. Solid State Chem. 167 (2002) 48–58.
[10] L.V. Makhnach, V.V. Pankov, P. Strobel, Mater. Chem. Phys. 111 (2008) 125–130.
[11] Z. Li, R. Haugsrud, T. Norby, Solid State Ionics 184 (2011) 42–46.
[12] J. Rodriguez-Carvajal, Physica B 192B (1993) 55–58.
[13] A. Marsh, Z. Kristallogr. 81 (1932) 285–287.
[14] W.A. Dollas, J. Appl Crystallogr. 19 (1986) 267–272.
[15] M. Gemmi, S. Nicolopoulos, Ultramicroscopy 107 (2007) 483–494.
[16] V. Vashook, E. Girdauskaite, J. Zosel, T.-L. Wen, H. Ullmann, U. Guth, Solid State Ionics 177 (2006) 1163–1171.
[17] K. Vidyasagar, A. Reller, J. Gopalakrishnan, C.N.R. Rao, Chem. Commun. (1985) 7–8.
[18] J.A. Alonso, M.J. Martinez-Lope, J.L. Garcia-Munoz, M.T. Fernandez-Diaz, J. Phys. Condens. Matter. 9 (1997) 6417–6426.
[19] Y. Gopalakrishnan, G. Colsmann, B. Reuter, J. Solid State Chem. 22 (1977) 145–151.
[20] I.F. Kononuck, N.G. Surmach, L.V. Makhnach, Inorg. Mater. 18 (1982) 1222–1225.
[21] X. Granados, J. Fontcuberta, M. Vallet-Regi, M.J. Sayagué, J.M. Gonzales-Calbet, J. Solid State Chem. 102 (1993) 455–464.